Frictional Melting Processes and the Generation of Shock Veins in Terrestrial Impact Structures: Evidence from the Steen River Impact Structure, Alberta, Canada

Erin L. Walton, Thomas G. Sharp, and Jinping Hu

Frictional melting processes and the generation of shock veins in terrestrial impact structures: evidence from the Steen River impact structure, Alberta, Canada.

Erin L. Walton[1,2]*, Thomas G. Sharp[3] and Jinping Hu[3]

[1]MacEwan University, Department of Physical Sciences, Edmonton, AB, T5J 4S2, Canada. [2]University of Alberta, Department of Earth & Atmospheric Sciences, Edmonton, AB, T6G 2E3, Canada. [3]Arizona State University, School of Earth & Space Exploration, Tempe, AZ, 85287-1404, USA.

corresponding author. Email address: waltone5@macewan.ca (E. Walton)

Keywords: Shock veins, Steen River impact structure, friction melting, majorite, shock metamorphism, high-pressure phases, cratering, mechanics

ABSTRACT

Shock-produced melt within crystalline basement rocks of the Steen River impact structure (SRIS) are observed as thin (1 – 510 µm wide), interlocking networks of dark veins which cut across and displace host rock minerals. Solid-state phase transformations, such as ferro-pargasite to an almandine-andradite-majorite garnet and amorphization of quartz and feldspar, are observed in zones adjacent to comparatively wider (50–500 µm) sections of the shock veins. Shock pressure estimates based on the coupled substitution of Na^{+}, Ti^{4+} and Si^{4+} for divalent cations, Al^{3+} and Cr^{3+} in garnet (14–19 GPa) and the pressure required for plagioclase (Ab_{62-83}) amorphization at elevated temperature (14−20 GPa) are not appreciably different from those recorded by deformation effects observed in non-veined regions of the bulk rock (14–20 GPa). This spatial distribution is the result of an elevated temperature gradient experienced by host rock minerals in contact with larger volumes of impact-generated melt and large deviatoric stresses experienced by minerals along vein margins.

Micrometer-size equant crystals of almandine-pyrope-majorite garnet define the shock vein matrix, consistent with rapid quench (100–200 ms) at 7.5–10 GPa. Crystallization of the vein occurred during a 0.1–0.15 s shock pressure pulse. Majoritic garnet, formed during shock compression by solid state transformation of pargasite along shock vein margins, is observed in TEM bright field images as nanometer-size gouge particles produced at strain rates in the supersonic field (10^6–10^8). These crystals are embedded in vesiculated glass, and this texture is interpreted as continued movement and heating along slip planes during pressure release. The deformation of high-pressure minerals formed during shock compression may be the first evidence of oscillatory slip in natural shock veins, which accounts for the production of friction melt via shear when little or no appreciable displacement is observed. Our observations of the mineralogy, chemistry and microtextures of shock veins within crystalline rocks of the SRIS allow us to propose a model for shock vein formation by shear-induced friction melting during shock compression.

1. Introduction

Shock veins in meteorites have received much attention owing to their association with minerals stable at high pressure and high temperature (e.g., Sharp and DeCarli, 2006; Gillet et al., 2007). Notably, shocked meteorites provide nearly all natural examples of deep Earth minerals, including the first reported natural occurrence of $MgSiO_3$ bridgmanite, the most abundant mineral in Earth, documented from shock veins in the Tenham L6 chondrite (Tomioka and Fujino, 1997, Tschauner et al., 2014). These high-pressure minerals, formed by crystallization from impact-induced melt or solid-state transformation of igneous precursors, constrain the P-T-*t* conditions experienced by the rocks during shock metamorphism; provide insight into the mineralogy of planetary interiors, and shed light on mechanisms of phase transformation. Similar features, explicitly linked to shock, have been documented from a few terrestrial impact structures including Manicouagan (Biren and Spray, 2011), Ries (Dressler and Graup, 1969; Stähle et al., 2011), and

Vredefort (Martini, 1978, 1991). Micro-pseudotachylites, the so-called S-type pseudotachylites of Spray (1998) and the A-type pseudotachylite of Martini (1991), or pseudotachylitic breccias formed as a result of shock compression (Reimold, 1998), are widely accepted as analogous to shock veins in meteorites, and for both shock-induced melt veins the term “shock veins” will be used (Stöffler and Grieve, 2007).

In this study a network of shock veins from the Steen River impact structure of Alberta, Canada is described. The mineralogy, composition and micro-textures of impact-induced phase transformations associated with shock veins constrain the P-T-*t* conditions during shock metamorphism and provide insight into the mechanisms involved in the formation of shock veins in crystalline rocks during a hypervelocity impact event. In addition to constraining the shock conditions, studies of shock veins in terrestrial impact structures also relate to meteoritics because they preserve the geological content of the rock within the crater structure, which is lacking in studies of these same features in meteorites. Here, high-resolution transmission electron microscopy has been applied for the first time to a novel shock-induced amphibole transformation, which has been documented previously from a single terrestrial impact structure (Stähle et al., 2011). This is the first reported occurrence of high-pressure minerals in the Steen River Impact Structure.

2. Geologic Setting of the Steen River impact structure

The Steen River impact structure (SRIS; 59^{o}31'N, 117^{o}39’W) is a buried complex crater in NW Alberta, Canada (Grieve, 2006) (Fig. 1), ascribed to hypervelocity impact based on the presence of shock deformation and transformation features in quartz and feldspar (Carrigy and Short, 1968; Winzer, 1972). The target rocks include 70 m of Mississippian calcareous shale underlain by ~1530 m of Devonian marine sedimentary rocks including evaporites, carbonates and shales. This ~1.6 km thick package of sedimentary rock overlies Lower Proterozoic crystalline rocks of the Hottah Terrane and Great Bear Magmatic Arc, thought to be joined along a faulted contact (Burwash et al., 1994). With a roughly elliptical shape and

~25 km diameter length, the SRIS is the largest known impact structure in the Western Canada Sedimentary Basin. This structure is of economic interest because it is an oil and gas producer and reservoir host (Grieve, 2006). A central uplift measuring 4 km at its top and 8 km at its base raises fractured basement 800–1100 m above regional levels (Winzer, 1972). The impact crater age, reported as 95 ± 7 Ma, is based on a single K-Ar whole rock age obtained from a 'pyroclastic vesicular rock' (Carrigy and Short, 1968). This rock represents an impact-melt bearing polymict breccia sampled in the allochthonous impactites of core IOE Steen 12-19-121-21 near the center of the structure. Although this age, recalculated using more recent decay constants of Steiger and Jager (1977) to be 91 ± 7 Ma, is roughly consistent with stratigraphic constraints, the SRIS remains a candidate for further isotopic analysis to better constrain this estimate on impact timing.

3. Materials and analytical methods

In early 2000, New Claymore Resources Ltd drilled three continuous but shallow diamond drill holes into the crater fill deposits of the SRIS (ST001, ST002, ST003). These cores are currently housed at the Mineral Core Research Facility in Edmonton (Molak et al., 2002). One hole, ST003, encountered ~154 m of melt-bearing polymict impact breccia (Walton et al., 2015). The lower 16 m sampled granitic basement; either the hole penetrated parautochthonous rocks of the central uplift or a large block in a basal breccia lying between polymict breccia and more massive rocks of the parautochthone or autochthone proper. Unfortunately this can only be resolved by deeper drilling. Three polished thin sections of shock-vein bearing rock were prepared from the ST003 core sampled at a depth of 378 m (within crystalline rocks at the bottom of ST003). These thin sections were examined by transmitted and reflected light microscopy, and via back-scattered electron (BSE) mode imagery with a Zeiss EVO MA 15 scanning electron microscope (SEM) with a LaB_6 filament at the University of Alberta. BSE images were acquired with a Si diode detector using a 20 kV accelerating voltage and a 7.5 mm working distance. This SEM is fitted with a Bruker silicon drift detector for energy dispersive spectrometry (EDS) analysis with a peak resolution of 125 eV. Commercial image analysis software, the freeware program ImageJ, was used to accurately measure apparent vein width and grain size on BSE images, and on photomicrographs acquired with the petrographic microscope. Major and minor elemental abundances of minerals were measured using a JEOL 8900 electron microprobe (EMP) at the University of Alberta, equipped with five wavelength dispersive spectrometers using an accelerating potential of 15 kV and a beam current of 10 nA. Most minerals were analyzed using a focused beam (1 µm) with the exception of beam-sensitive feldspars. To minimize alkali element migration in this beam-sensitive material a defocused (10 µm) beam was employed. Natural minerals were used as standards and raw data were corrected by the ZAF procedure. X-ray elemental maps were obtained on select areas of the thin section using the JEOL 8900 EM with an accelerating voltage of 20 KV and a beam current of 20 nA. The excel spreadsheets of Locock (2008, 2014) and Grew et al. (2013) were used to recast chemical analysis of garnets and amphiboles following IMA recommendations. Micro-Raman spectra of various phases were obtained using a Bruker SENTERRA instrument at MacEwan University, operating with an Ar+ laser of 532 nm wavelength. The focal spot size was ~1 µm. Two areas of interest were excavated by focused ion beam (FIB) lift-out using a FEI Nova 200 NanoLab at Arizona State University. FIB sections were examined by transmission electron microscopy (TEM) imaging and selected area electron diffraction (SAED) using an FEI CM200-FEG analytical TEM instrument housed at the LeRoy Eyring Center for Solid State Science at Arizona State University. The TEM was operated using an accelerating voltage of 200 kV.

4. Results

Shock metamorphic effects may be described as deformation, transformation or a combination of these two processes. There is a distinct difference between those effects manifest in the bulk rock and those adjacent to, and in clasts entrained within, the shock veins. The crystalline basement rock, as represented by the ST003 core between 362–378 m, is plagioclase-orthoclase-quartz-amphibole-biotite gneiss with minor apatite, titanite, zircon, epidote, ilmenite and chlorite (Fig. 2a). Representative chemical analyses of major minerals are given in Table 1. The compositional range of plagioclase spans andesine to albite, $An_{9.4-36.5}Ab_{62.2-83.3}Or_{0.8-8.9}$. Orthoclase is $An_{0-0.5}Ab_{11.7-25.5}Or_{74.4-81.1}$. Quartz and feldspar within the host rock (>0.5 mm from shock veins), are pervasively fractured and exhibit moderate to strong mosaicism under cross polarized light (Fig. 2b). Fractures in these minerals occur as irregular networks and planar fractures (PFs; Fig. 2c). Quartz has a slight brown "toasted" discoloration, with up to two sets of planar deformation fractures (PDFs) with distinct crystallographic orientations observed in a single grain (Fig. 2d). Amphibole in the host rock (0.4–2 mm) is pleochroic in shades of green, yellow-green and brown. EPMA results show that it is ferro-pargasite with the formula $(Na_{0.41}K_{0.27})(Ca_{1.82}Na_{0.10}Mn_{0.08})(Fe^{2+}_{3.04}Mg_{1.33}Al_{0.29}Ti_{0.19}Fe^{3+}_{0.14})(Si_{6.60}Al_{1.40})O_{22}(OH)_2$, calculated using the spreadsheet of Locock (2014) and following IMA recommendation (Table 1).

Host-rock minerals are cross cut by a network of interlocking, curvilinear to straight veins ranging in apparent width from 1 µm up to 510 µm (Fig. 2a). Displacement along the vein margin is observed as micro-scale offset of igneous minerals (Fig. 3). Measured apparent displacement range from 20 µm to 200 µm. Plagioclase and quartz in direct contact with wider portions of the shock vein are partially isotropic forming diaplectic glasses along shock vein margins and exhibit a much more extensive degree of replacement by secondary minerals (mostly clays) compared to shocked crystalline grains in non-veined regions of the host rock (Fig. 2b). Within a zone ~100–300 µm wide along the shock vein margin, a striking transition from green amphibole to a bright orange mineral is observed in transmitted light (Fig. 4a). EMP analyses, Raman spectroscopy and TEM SAED patterns collected on this orange mineral confirm that it is an almandine-andradite-majorite garnet (Table 1, Fig. 6), with a representative formula of $(Fe_{1.37}Ca_{0.97}Mg_{0.42}Na_{0.2}Mn_{0.05})(Al_{0.92}Si_{0.36}Fe_{0.35}Mg_{0.22}Ti_{0.10})Si_3O_{12}$. Silicon ranges from 3.35–3.39 cations per formula unit. Based on the excess silicon atoms, this garnet contains a 35–39% majorite component. These garnets contain a significant amount of sodium (0.99–1.36 wt% Na_2O) and potassium (0.32–0.92 wt% K_2O). In BSE images, garnets exhibit a complex network of curved cracks, with fingers of garnet extending into pargasite along cleavage planes (Fig. 4b, c). It is noted that the phase transformations described here (plagioclase and quartz → glass, pargasite → garnet) are only observed in those grains in direct contact with wider portions of the shock veins (50–500 µm). Phase transformations are not observed in host rock minerals in direct contact with shock veins that are essentially melt-coated faults (1–4 µm wide; Fig. 3).

The matrix of the shock vein is opaque in plane light, ranging from black, reddish-brown to grey (Fig. 4a). BSE images show the interior texture to be fine-grained (≤2 µm) and granular (Fig. 4d). The largest micrometer-size crystals were analyzed with Raman and EMP, and found to be almandine-pyrope-majorite garnet, $(Fe_{1.54}Mg_{1.31}Ca_{0.05}Na_{0.04}Mn_{0.03})(Al_{1.81}Si_{0.11}Mg_{0.04}Ti_{0.03})Si_3O_{12}$ (Table 1, Fig. 6), with 11–22% majorite component based on the number of excess silicon atoms per formula unit. Like in the orange garnet along shock vein margins, sodium and potassium contents are significant (0.13–0.77 wt% Na_2O and 0.33–0.94 wt% K_2O). Raman spectra collected on the vein matrix show peaks at ~360 cm^{-1} and 910 cm^{-1}, consistent with majoritic garnet as the main mineral (Fig. 6). Bright-field TEM images were acquired on two FIB foils, one sampling the fine-grained minerals at the shock vein margin and the other poikilitic crystals in the center of the wider (0.5 mm) vein (Fig. 4 e-g, Fig. 5). Both show that the shock vein matrix consists of garnet + phyllosilicates + amorphous material. Bright field images show round inclusions within garnet that have bright contrast and curved layered structures (Fig. 4 e-g). These are interpreted to be glass inclusions partially altered to phyllosilicates. SAED patterns show that the garnets in the shock vein matrix are cubic with a relatively large unit cell (~11.84 Å). Similarly, SAED patterns indicate that the phyllosilicates are mostly chlorite (d_{001} = 14.2–14.5 Å) with some smectite (d_{001} = 11.6 Å). Amorphous material is identified by a series of diffuse rings, which appear in SAED patterns.

One FIB section was extracted across the interface between the orange almandine-andradite-majorite garnet and the shock vein matrix (Fig. 5a,b). The garnet at the shock vein margin is not a single crystal, but consists of nanometer size crystals (100–550 nm) surrounded by vesiculated glass (Fig. 5c, d). This texture corresponds to the fragmented texture observed in BSE images (Fig. 4b). In TEM bright field images, the angular nanometer size garnet fragments have complementary shapes that, if pushed together, would tessellate into a continuous space filling mass (Fig. 5d). The fragments have nearly uniform diffraction contrast indicating that they are similarly oriented. These similarly oriented fragments that fit together suggest that they were originally part of a single garnet crystal that was subsequently fragmented. Several grains of deformed and partially melted biotite were also encountered within this zone (Fig. 5d).

5. Discussion

5.1 Formation mechanisms of majoritic garnet at the SRIS

The occurrence of majorite-bearing garnet is restricted to those areas of the host rock where amphibole is cut by shock veins, and are absent in non-veined regions of the host rock. The composition, grain size and texture of shock-produced garnets – grains bordering shock vein margins and those garnet grains that define the shock vein matrix – are distinct, implying they formed by different mechanisms. Garnet crystals within the shock vein matrix are fine-grained, ≤2 µm, equant subhedral to euhedral crystals embedded within amorphous material and phyllosilicates (chlorite + smectite) (Fig. 4d-g). The larger grains poikilitically enclose round amorphous inclusions, some with sheet structure. The amorphous material and poorly crystalline phyllosilicates suggest alteration of a glass phase. These garnets have an almandine-pyrope-majorite composition, excess silicon, a significant amount of sodium and potassium, and are interpreted to have crystallized from shock melt at high pressure. In contrast, the almandine-andradite-majorite garnet at the shock vein margin have a larger amount of excess silicon (3.35–3.39 cations Si per 12 O versus 3.11–3.22 cations Si per 12 O) and therefore a higher majorite component (35–39% versus 11–22% majorite), as well as greater sodium content (0.99–1.36 wt% Na_2O versus 0.13–0.77 wt% Na_2O). Both garnet occurrences contain significant potassium (0.32–0.92 wt% K_2O versus 0.33–0.94 wt% K_2O). The orange garnet formed along the shock vein margin is interpreted to have formed by a solid-state reconstructive transformation of amphibole during shock compression. Textures are consistent with formation at high temperatures by nucleation and growth (Sharp and DeCarli, 2006), but the fragmented nature of the garnet that we observed makes interpretation of transformation mechanisms difficult (Fig 5d). The large quantities of alkali metals in solid-state transformed garnets are inherited from the pargasite precursor by transformation at high pressure and those in the shock vein matrix, by rapid crystallization from a high-pressure melt. It should be noted that some of the alkalis and silica detected in EMP analysis of those garnets that crystallized from shock melt may be attributed to the tiny glass inclusions visible in TEM bright field images (Fig. 4f) but not readily apparent in BSE images (Fig. 4d).

The spatial association between garnet and the shock vein, and the absence of this mineral in non-veined regions of the host rock, indicates that the garnet in the SRIS samples formed during hypervelocity impact. In both occurrences (adjacent to and within shock veins) excess silicon accommodated in octahedral sites in the crystal structure is indicative of formation at high pressure, which is well-documented experimentally (e.g., Ringwood 1967). The incorporation of sodium into the crystal structure of garnet can occur by the following substitution: ${}^{X}Na^{1} + {}^{Y}R^{4+} \rightarrow {}^{X}R^{2+} + {}^{Y}R^{3+}$, which introduces sodium and ${}^{[VI]}Si$ into the garnet group. The Na and K in the shock-produced garnets are consistent with their formation at high pressure (Grew et al., 2013). Under conditions of ultrahigh temperature metamorphism but (comparatively) low pressure such as those experienced by granulite and amphibolite facies rocks (>900

^{o}C; 10 kbar / 1 GPa), pargasite breaks down to form a symplectitic assemblage of orthopyroxene + clinopyroxene + plagioclase + ilmenite ± apatite (Sajeev et al., 2009). Evidence of such thermal decomposition was not encountered in our detailed characterization of SRIS shock veins, further supporting that the pargasite transformation occurred during shock compression under high pressure and elevated temperature conditions.

EMP data were collected on pargasite-almandine crystals in direct contact with each other (Fig. 7). Inputting wt% oxide abundances of solid-state transformed pargasite (to garnet) into the amphibole spreadsheet of Locock (2014) assigns this composition to "ferro-ferri-hornblende" species with $Fe^{3+}/\sum Fe$ = 0.19–0.24 and 1.94–1.95 wt% H_2O, calculated based on stoichiometry. If the transformation was 100% isochemical, then the composition would be assigned as ferro-pargasite, identical to that of untransformed amphibole in the host rock. It should be noted that the water content may be an overestimate as the amount of H_2O in the original pargasite was 1.84–1.87 wt% H_2O (calculated using the same method); however, the hydrous nature of the solid-state transformed garnets is supported by consistently low totals obtained in EMP analyses (96.1–98.6 wt% oxides, n = 36) and by previous ion probe analysis of shock-produced garnet (Stähle et al., 2011). At the Ries crater, Germany, Stähle et al. (2011) demonstrated that shock-transformed hornblendes (to majorite-bearing garnet) are hydrous, with 0.7–0.9 wt% H_2O. In contrast, EMP totals for quench-crystallized garnets in the vein matrix of our sample are close to 100% (99.2–100.5 wt% oxides). This indicates that these garnets are anhydrous, consistent with a distinct formation mechanism (crystallization from shock melt) compared to those hydrous grains transformed in the solid state from pargasite. Another interesting observation is the calculated amount of oxidized iron in the garnet structure ($Fe^{3+}/\sum Fe$ = 0.19–0.24) compared to the original pargasite ($Fe^{3+}/\sum Fe$ = 0.039–0.078). We therefore conclude that although the almandine-majorite garnet formed from pargasite by solid-state transformation, the transformation was not isochemical, with loss of volatile species Na, K and Cl and shock-induced oxidation of iron.

5.2 Constraints on shock pressure from garnet composition

Majorite is the alumina-depleted variety of the garnet supergroup, which forms at sub-lithospheric mantle pressures (Ringwood, 1967). The composition of garnet is strongly pressure dependent (Akaogi and Akimoto, 1979; Irifune 1986; Nishihara and Takahashi, 2001). A single-phase method for pressure estimates based on the coupled substitution of Si^{4+} + Ti^{4+} for Al^{3+} and Cr^{3+} in octahedral coordination sites of the crystal structure has been widely applied (Stachel, 2001; Xirouchakis et al., 2002; Griffin, 2008; Collerson et al., 2010; Stähle et al., 2011). Here, a pressure estimate of 14.6–15 GP is obtained for the almandine-andradite-majorite garnet observed in our samples from the SRIS using the relationship between Al + Cr and Si of Stachel et al. (2001). A slightly lower pressure of 7.5–10 GPa is estimated by applying the same calibration to the garnets that formed by crystallization from shock melt. The experimentally determined fit between silicon content and pressure, presented by Xirouchakis et al. (2002), results in similar formation pressures of 14–15 GPa and 7–10 GPa for solid-state transformed and quench-crystallized garnets, respectively. In addition to silicon and titanium, experimental studies have shown that the sodium content of garnets with majoritic chemistry is also pressure-dependent and is therefore a potential geobarometer. Using the coupled substitution of Na^{+}, Ti^{4+} and Si^{4+} for divalent cations (M^{2+}), Al^{3+} and Cr^{3+}, Collerson et al. (2010) developed a means for estimating pressures based on experimental data for different bulk compositions using the following equation:

$$P\ (\mathrm{GPa}) = 5.78 + (18.23 * X^{cat}Mj)$$

where $X^{cat}Mj = X^{cat}Mj_{(1)} + X^{cat}Mj_{(2)}$ and $X^{cat}Mj_{(1)} = [^{IV,VI}(Si + Ti) - 3 + {}^{VIII}Na]$, and $X^{cat}Mj_{(2)} = [1 - 0.5 * {}^{VI}(Al + Cr)] + {}^{VIII}(Na * 1.25)$. This method also enables calculation of the error in pressure based on the expression Error (GPa) = $SD[(X^{cat}Mj_{(1)} + X^{cat}Mj_{(2)})] * 18.23$. The silicic majoritic garnets from the SRIS interpreted to have formed by solid state transformation from amphibole, with X^{cat}_{Mj} content ranging from 0.673 to 0.752 give a pressure range of 18.0 ± 2.1 GPa and 19.4 ± 1.6 GPa. Those garnets with majorite chemistry which have crystallized within shock veins with X^{cat}_{Mj} of 0.159 to 0.205 yield lower pressure estimates, ranging from 8.6 ± 0.52 GPa to 9.4 ± 0.90 GPa. Pressure estimates from garnet composition are summarized in Table 1.

5.3 Shock pressure constraints from plagioclase

The coexistence of crystalline and amorphous plagioclase in crystalline basement rocks of the SRIS suggests a moderate shock pressure. The static compression experiments of Kubo et al. (2010) and Tomioka (2010) demonstrate that the response of plagioclase to shock is strongly dependent on composition, as shown by earlier studies on experimentally shocked feldspar (Stöffler 1974; Ostertag 1983) and more recently by Fritz et al. (2011a). Kubo et al. (2010) used $An_{0.4}Ab_{98.0}$ and $An_{51.8}Ab_{45.0}$ as starting material for their experiments, while Tomioka et al (2010) use crushed natural albite crystals (Ab_{98}) as their starting products. The plagioclase compositions in our thin sections ($An_{9.4-36.5}Ab_{62.2-83.3}$) are intermediate between the experimental starting and we therefore estimate the shock pressure using this calibration to be ~14–20 GPa, which overlaps with the ~15–19 GPa required to produce the majorite-bearing garnets (section 5.2). According to the progressive stages of shock metamorphism described by Stöffler (1971, 1984) for shocked quartzo-feldspathic rocks, deformation in the bulk rock (e.g., planar deformation features in quartz) classifies those SRIS rocks described in this study as stage 1a. The shock pressures and temperatures required to produce this deformation, calibrated from shock-recovery experiments, is ~20 GPa accompanied by a post-shock temperature increase of 170 ^{o}C. Assuming burial at ~2 km and a geothermal gradient of 25 ^{o}C/km, the post-shock temperature in the host rock would have been ~220 ^{o}C. Therefore, the crystalline basement rocks as represented by this sample reached a shock pressure of ~14–20 GPa and a post-shock temperature (away from shock veins) of 220 ^{o}C. It is therefore reasoned that the shock pressure required to produce the phase transformations associated with shock veins are not appreciably different from those conditions required to produce shock effects in the bulk rock. This is relevant to the model presented for shock vein formation in section 5.7.

5.4 Constraints on the formation of shock veins

The phenomenon – whereby high pressure minerals such as wadsleyite, ringwoodite, majorite, stishovite occur almost exclusively in and around shock melts – is well known from studies of shock metamorphism in meteorites (e.g., Langenhorst and Poirier, 2000; Beck et al., 2005; Xie et al., 2006). In our samples of crystalline basement rocks from the SRIS the same spatial association between shock veins and mineral transformation is documented. A significant observation is that phase transformations (amphibole to garnet; tectosilicates to glasses) are only observed along the margins of shock veins where larger volumes of impact-generated melt are produced (i.e., where apparent vein width exceeds 50 µm). Host rock minerals along the thinnest shock veins (1–4 µm) exhibit deformation features such as development of planar fractures and mosaicism, but whole grain transformation products (i.e., diaplectic glasses replacing precursor minerals) are not observed (Fig. 3a-d). Here, we investigate the hypothesis that the amount of heat available is driving phase transformations. This is relevant to the formation of shock veins, as previous models for shock vein formation have called upon anomalously high pressures along vein margins to initiate phase transformation which is not supported by our observations (see discussion in section 5.8). If pressure were the only important factor driving phase transformations, they would be observed along the margins of all shock veins, regardless of the amount of shock melt produced.

According to the experimental data of Kubo et al. (2010), wherein *in situ* synchrotron micro X-ray diffraction experiments were carried out on synthetic mineral powders of albite-rich (Ab_{98}) and intermediate composition (Ab_{45}) plagioclase, partial amorphization of albite and labradorite at low temperature takes place at 35 GPa and 22 GPa, respectively. Experiments carried out at elevated temperature demonstrated the inverse relationship between the pressure at which amorphization begins and temperature. For example, at 500 °C, the boundary between complete and partial amorphization of albite is ~29 GPa and of labradorite, ~14 GPa (Figure 1; Kubo et al. 2010). One major limitation in directly applying this data to naturally shocked materials such as our SRIS samples is that the amorphization transitions were observed under static compression. Naturally shocked rocks have experienced both shock compression and decompression upon arrival of the release (rarefaction) wave. Observations of the recovered samples from static compression experiments by Tomioka et al. (2010) using crushed albite crystals ($Ab_{98.8}$) showed that when compressed at room temperature and upon compression with heating to 170 °C, albite amorphization was initiated between 26 and 32 GPa, and is complete at 37 GPa. At higher temperature (270 °C), the amorphization pressure dropped to 31 GPa. The influence of temperature on quartz deformation and transformation has been recently investigated in the shock recovery experiments of Fritz et al. (2011b) in which quartz crystals were precooled to 77 k. Similar to the results of Tomioka et al (2010) in their investigations of albite, Fritz et al. (2011b) demonstrated that the response of quartz to shock was temperature insensitive below 275 °C but sensitive to temperatures above this threshold up to 630 °C. For example, complete amorphization was achieved at shock pressures of 35 GPa and 36 GPa in the room temperature and pre-cooled quartz targets, respectively. At elevated temperatures the onset of amorphization was lowered by 7 GPa (to 28 GPa) in the 540 °C runs and by 9 GPa (to 26 GPa) in the 630 °C pre-heated runs (Fritz et al., 2011b). Thus for both tectosilicates in our SRIS samples – quartz and feldspar – it is well established through static high pressure experiments and shock recovery experiments that the onset of amorphization is temperature dependent.

Another insight into the spatial distribution between shock veins and mineral transformations lies in the static compression experiments of Daniel et al. (1997), who studied the high-pressure behaviour of anorthite up to 30 GPa. These experiments examined not only the behaviour of feldspar on increasing pressure under hydrostatic conditions, but on the ability of the crystal structure to recover after pressure release. In their runs only those crystals experiencing pressure >22 GPa remain amorphous after pressure release. Daniel et al (1997) also examine the behaviour of anorthite under less than hydrostatic stress conditions and found that the onset of transition is strongly sensitive to shear stresses. Compared to anorthite powders compressed under hydrostatic conditions, the onset of amorphization was lowered from 16 GPa to 11 GPa, demonstrating the importance of shear stress in determining the response of minerals. Such conditions are of relevance to the shock veins in this study, which form by shear-induced frication melting (section 5.5) and relate to our model of shock vein formation, discussed in section 5.7.

5.5 Formation of shock veins by friction melting along shear bands

Shock veins may form by a number of distinct mechanisms including shock wave collisions, friction heating along shear bands, or by the interaction of shock waves with void space (e.g., fractures, cracks, pores) during shock compression (Stöffler, 1974; Sharp and DeCarli, 2006). Shock collisions due to grain-scale heterogeneities are predicted to form narrow veins in minerals of low shock impedance (shock wave velocity x mineral density) like feldspar. The shock veins observed at the SRIS are formed in feldspars and quartz, but also high shock impedance minerals (amphibole) and are therefore not accounted for by this mechanism. Differentiating between those shock melts produced by collapse of void space and friction melts, the latter analogous to pseudotachylites, is difficult; however, several observations point to the formation of the shock veins at the SRIS by shear-induced friction melting. These include the bulk composition of the shock vein, offset and displacement of igneous minerals, ultracataclastic textures at vein margins and comparison with experimentally-produced shear melts.

Crystallization of an almandine-pyrope-majorite garnet from melt indicates that the bulk composition of the shock vein is not that same as the host rock, i.e., the melt composition is more ferromagnesian and less siliceous than would result from bulk melting of plagioclase-orthoclase-quartz-pargasite-biotite gneiss. Such discrepancies in bulk composition are typical of friction melts where melting does not proceed according to the melting temperature of individual minerals, but instead is dependent on fracture toughness, K_c (Spray, 2010). The K_c of major minerals in the SRIS host rock are quartz (1.6–2.4) > orthoclase (0.9–1.3) > plagioclase (0.75) > amphibole (0.76) > biotite (0.2). Therefore, the enrichment of friction melt in inosilicates and phyllosilicates is not only expected, it is predicted. As noted by Walton et al. (2005) with increased volumes of melt the composition approaches that of the bulk rock. Thus, the small volumes of melt sampled here from <0.5 mm wide shock veins are expected to show large deviations from the bulk rock composition.

Apparent displacement of host rock minerals are observed as micro-scale offsets (20 – 200 μm) along vein margins (Fig. 3). This indicates a shear component to shock vein formation at the SRIS. Experimentally-produced shear melts possess many characteristics akin to those investigated in this study; they show strong variation in thickness, sudden changes in vein orientation, sharp vein contacts and mineral offset along their margins (Kenkmann et al., 2000).

In bright field TEM images the shock-produced almandine-andradite-majorite garnet along the vein margin is itself deformed, forming an ultracataclastic texture of nm-size crystals (Fig. 5). The production of gouge particles smaller than 1 μm and the large amounts of energy required to produce such a texture (100–1000 kW ton^{-1}; Lowrinson 1974) are consistent with shock vein formation during compression within the supersonic field at strain rates 10^6–10^8 (Spray, 2010). It is interesting to note that the 100–500 nm size garnet fragments produced in the SRIS pseudotachylite is below the 1 μm "comminution limit" or "grind limit". This supports the idea that this limit to fragment size is apparent; previous studies were not afforded the high resolution provided by TEM imaging (Chester et al., 2005).

Using the line of reasoning outlined in the preceding paragraphs, the shock veins have formed *in situ* by a combination of shock and friction. In order to use this to refine a model for shock vein formation in terrestrial impact structures, several other observations should be considered. These are: 1) submicron angular fragments of garnet along shock vein margins are surrounded by vesiculated glass, 2) slightly lower shock pressures are recorded by almandine-pyrope-majorite garnet which has crystallized from shock melt (7–10 GPa) compared to phase transformations which have occurred along vein margins (14–20 GPa) such as pargasite → almandine-andradite-majorite garnet and amorphization of plagioclase and quartz, and 3) although the shock vein formed *in situ* by preferential melting of double chain silicates (pargasite) and phyllosilicates owing to their low fracture toughness, apparent displacement along the fault is negligible (up to 200 µm measured by apparent displacement of igneous mineral along vein margins).

The first observation indicates that although slip was initiated during compression, deformation continued during pressure release to produce an ultracataclastic texture from shock-produced garnets and initiate incipient melting at low pressure to produce bubbles. The second observation is a well-documented phenomenon from shock veins in meteorites, attributed to the relationship between the shock duration (elapsed time between arrival of the shock wave and decompression), and the time it takes for the shock melt to crystallize by conduction of heat to the surrounding cooler host rock (Xie et al., 2006; Walton et al., 2014). In order to examine how the relationship between vein quench time and shock duration are related to samples from the SRIS, the conditions of impact required to produce a 25-km diameter complex crater must first be constrained. To produce a complex crater the size of the SRIS, the projectile may have had a diameter of 1–1.5 km depending on projectile type and velocity (Dence et al., 1977; French, 1998). The relationship $D_{impact} = \tau \times \upsilon$, where D_{impact} is the diameter of the impacting body, υ = impact velocity (10 km s^{-1}) and τ = shock duration, results in a calculated maximum shock duration of 0.1–0.15 s. Frictional melting occurs under adiabatic conditions, and the heat generated is dissipated by conduction of heat to the surrounding colder rock. Thermal models of Shaw and Walton (2013) for cooling and quench crystallization of shock melts in natural samples, demonstrate that the size (width), geometry (vein versus pocket) and spatial distribution of shock melts are important in determining the time it will take for a shock melt to cool below 900 ^{o}C. The time calculated for a 0.6 mm wide vein (the upper limit for shock vein width in the SRIS samples), to quench is 0.1–0.2 s. Here quench is defined as the time between peak temperature and the solidus at 25 GPa. The calculated shock pulse duration (0.1–0.15 s) is therefore on the same order as the modeled quench time for the melt (0.1–0.2 s). These calculations predict that the melt generated along the shock veins should have quenched at high pressure or during pressure release. Crystallization during pressure release is consistent with the lower pressure recorded by the vein mineral assemblage (Table 1; Fig. 8). Movement along the fault surface continued after decompression, which brecciated the solidified majoritic garnet along the shock vein margin and resulted in incipient melting at low-pressure to produce bubbles in glassy matrix (Fig. 5d). This leads directly to the third observation, namely that apparent displacement along the fault surface is negligible. This relates to the nature of slip on fault surfaces, which can be unidirectional or oscillatory. Our observations of high pressure mineral formation, brecciation and vesiculation may suggest the formation of shock veins in the SRIS rocks via oscillatory slip, where the small measured displacements are the total or integrated motion along the fracture slip system.

The observation of multiple phases of deformation on a single fracture-slip surface is significant because it is able to account for the production of friction melt via shear even when there is little to no appreciable displacement observed. For example field studies undertaken on pseudotachylitic breccias at the Vredefort Dome, South Africa, have called on injection from the melt sheet to explain their origin because small displacements / offsets along their margins are difficult to reconcile with a frictional melting origin (Lieger et al., 2009). While the thin shock veins investigated in this study from the SRIS are not directly comparable to those thick (meter-wide) veins at Vredefort where the large volumes of melt generated decrease the efficiency to produce frictional melt, it could serve as a cautionary note to field workers where the actual slip distance measured in outcrop may not represent the true amount of displacement.

5.6 Temporal constraints on shock-vein formation

In the same ST003 core sample from which the thin sections were prepared, a 2–6 mm wide veinlet of melt-bearing polymict breccia cuts across and truncates the shock vein (Fig. 8). The breccia matrix contains, in addition to shocked mineral and lithic clasts predominantly derived from the crystalline basement rocks, entrained clasts of the shock vein matrix. These are observed as 20–200 µm angular clasts of fine-grained almandine garnet, identical in size, shape and composition to those majorite-bearing garnets that have crystallized from shock melt (Fig. 8). This constrains the timing of shock vein formation and solidification prior to injection of the breccia veinlet. Similar breccias have been described from other impact structures, notably the "dike suevite" described from the Ries Crater, Germany, which forms by injection of a turbulent mixture of comminuted basement rock and minor impact melt clasts into the fractured basement rocks (Stöffler et al., 2013). The timing of dike suevite emplacement occurs toward the end of transient crater formation (after 15–20 s; Artemieva et al., 2013).

5.7 A model for shock-vein formation

This is the first study to investigate the mineralogy and microtextures of shock veins in a terrestrial impact structure at the nanometer scale. Our results provide critical constraints on the mechanism of shock vein formation that improve upon previous work. Based on the petrographic observations outlined in sections 5.4 and 5.5, a model for the formation of shock veins in terrestrial impact structures is proposed.

The network of shock veins in crystalline basement rocks from the SRIS were initiated during the contact / compression stage of crater formation as the shock wave propagated through the rocks. Micro-faulting and shear generated local hot spots along slip planes. The crystalline basement rocks at >1.6 km depth experienced an equilibration shock pressure of 14–20 GPa. The bulk of the rock experienced a post-shock temperature of ~220 ^{o}C (section 5.3), while the vein interior could have reached a minimum temperature of 2300–2500 K, constrained by experimentally produced shear melts (Kenkmann et al., 2000; Langenhorst et al., 2002). The heat transferred across the shock-vein interface into adjacent host rock minerals was high enough to overcome the kinetic barriers for solid-state phase transformations, forming majoritic garnet from pargasite. The case for amorphization of plagioclase and quartz is more complicated. In contrast, to the formation of high-pressure phases such as majorite-bearing garnet which require high temperatures, the formation of diaplectic tectosilicate glasses can occur at low temperature, as demonstrated by the experimental work of Fritz et al. (2011b) and is more constrained by the physical stability of the crystal lattice to survive high pressures (see also Fritz et al., 2011a). The temperature difference between the shock vein and host rock determined the rate of quench, which is estimated to have been 0.02 s from thermal models of similar size shock veins in meteorites. Micrometer-size almandine-pyrope-majorite garnet crystallized from the shock melt at the equilibration shock pressure or during pressure release. Continued movement along the fault following arrival of the release wave caused local deformation of earlier-formed high-pressure minerals along the vein margin. The solidified shock vein was cut across by a later melt-bearing polymict breccia veinlet, likely injected into the crystalline target rocks toward the end of transient crater formation (15–20 s).

5.8 Comparison with previous models for shock vein formation

Our model for shock vein formation applies to the features described here from crystalline target rocks of the SRIS and similar features in other terrestrial impact craters (Dressler and Graup, 1969; Martini, 1978, 1991; Reimold, 1998; Spray, 1998; Biren and Spray, 2011; Stähle et al., 2011). However, we acknowledge that different mechanisms may be responsible for the production of shock melt. These include pore collapse, jetting along cracks and pores, and shock wave collision in low-impedance minerals (e.g., Stöffler, 1974; Sharp and DeCarli, 2006). Our model differs from the previous models of shock vein formation, namely that of Biren and Spray (2011) in several important ways. Biren and Spray (2011) describe a network of shock veins within the central uplift of the Manicouagan impact structure, with which maskelynite (diaplectic feldspar glass) and stishovite are associated. In their model of shock vein formation the mineral transformations observed along vein margins (quartz → stishovite, feldspar → maskelynite) are regarded as shock "excursions", formed by higher shock pressures (12–30 GPa) concentrated along shock veins, and which deviate from relatively low shock pressure recorded by shock deformation effects in the host rock (≤ 12 GPa). The largest departure from the Biren and Spray (2011) model is that the phase transformations along shock vein margins are not attributed to anomalously high shock pressures concentrated along vein margins. Instead, it is *pressure, heat and deviatoric stresses* that drive phase transformations. Although tortuosity in the shock wave front, as it travels through heterogeneous materials such as rock composed of minerals with varying shock impedance, may be responsible for generating slip systems through shear stress (Kenkmann et al., 2000; Heider and Kenkmann, 2003; Gibson and Reimold, 2005), these pressure gradients are transient and ring out very quickly. The computational modelling of Baer (2000) and Baer and Trott (2002) demonstrated that the time required for pressure equilibration is less than a microsecond. Therefore, although pressure heterogeneities may be experienced by the rock upon arrival of the shock wave, complex interactions between shock waves equilibrate the pressure on a much shorter time scale than the expected shock duration in natural impact events. Solid-state phase transformation and impact-induced melt generation and quench-crystallization take place during the shock pulse (0.1–0.15 s). Secondly, in our model melting occurs during shock compression, at high pressure, in contrast with melting upon rarefaction (Biren and Spray, 2011). Crystallization of shock veins under nearly constant equilibrium shock pressure conditions is well-known from meteorite studies, and heavily shocked L-chondrites in particular (e.g., Chen et al., 1996; Xie et al., 2006), where mineral assemblages of similar pressure stabilities are found throughout a given shock vein. Melt in shock veins may then crystallize during or following decompression, if the timing of quench crystallization is shorter than the short duration (Xie et al., 2006; Walton et al., 2014). The current study demonstrates that localized deformation and shock-vein formation can also occur during or after decompression.

5.9 Implications for the shock history of meteorites

One motivation for the study of shock metamorphic effects in meteorites is to deduce how many impact events are required to explain the observed deformation and transformation features. This relates to the interpretation of ages from the samples (crystallization versus shock-resetting) and to the size and frequency of impact events on their parent body. Temptation exists to assign multiple impact scenarios to meteorites when complicated micro-scale shock features are observed (Treiman, 1998). Although the generation of shock veins may be thought of as the result of a single, unidirectional slip event, this study demonstrates the deformation of a shock-induced high pressure phase in a single impact event, which implies multiple stages of movement along the slip surfaces during impact. Such textures are not inconsistent with the complex deformation processes in an impact event. This serves as a cautionary note to meteoriticists; shock is a complex process and can lead to extremely complicated textures when observed on the micrometer to nanometer scale.

6. Summary and Conclusions

In this study we document a novel shock-induced amphibole to garnet phase transformation in the Steen River impact structure, which has previously been reported from a single terrestrial impact crater. The composition of majoritic garnet formed during shock wave passage through the crystalline basement rocks of this 25 km diameter complex crater record shock pressures on the order of 14.6 – 19.4 GPa. This pressure estimate is not appreciably different from shock pressures recorded by deformation and transformation effects in non-veined regions of the bulk rock (14 – 20 GPa) calibrated from shock recovery experiments, or from the observed amorphization of tectosilicates in contact with the shock veins. Focused ion beam foils extracted across the shock vein margin demonstrate that solid-state, impact-induced high pressure phases are themselves deformed in a late event which quenched vesicular glass. This is consistent with multiple stages of deformation and melting. The micrometer-scale direction of movement recorded by the offset and displacement of minerals along shock vein margin may be the total integrated motion of oscillatory movements along the fracture slip system. The detailed characterization of shock-veined crystalline rocks from a terrestrial impact structure improves upon previous models for the mechanism of shock-vein formation. In our model shock veins form by deformation along shear bands and friction melting during shock compression, which does not require local pressure excursions to explain the association between phase transformation and shock veins. Instead, heat and deviatoric stresses are regarded as important factors governing the phase transformations that are exclusively associated with shock veins.

Acknowledgements

Financial support for this project was provided by NSERC Discovery Grant RES00007057 awarded to ELW and NASA Cosmochemistry Grant NNH08ZDA001B-Cos awarded to TGS. We gratefully acknowledge the use of the FIB/TEM facilities within the LeRoy Eyring Center for Solid State Science at Arizona State University. Thanks to Andrew Locock and Martin von Dollen at the University of Alberta for expertise in electron microprobe and sample preparation, respectively. Rob Natyshen, Gordon Jean and Diane Goulet at the Mineral Core Research Facility and Tyler Hauck (Alberta Geologic Survey) are thanked for their assistance with core sampling. We thank Mark Norman for editorial handling, and Uwe Reimold and Jörg Fritz for insightful reviews, which improved the quality of this manuscript.

Figure and table captions

Fig. 1. Simplified geological map showing the location of the Steen River Impact Structure (SRIS) at 59° 30' N, 117° 38' W, superimposed on the structure of the lower Proterozoic crystalline basement rocks (modified after Burwash et al., 1994). The structure is somewhat asymmetric, measuring ~25 km in length defined by a concentric raised rim forming a 20–50 m positive feature. The syncline locally downthrows basement rocks by >500 m. The central uplift measures 8 km at its base and 4 km at its top. The whole structure is surrounded by a disturbed zone extending 30 km from the crater center (not shown).

Fig. 2. Thin section of crystalline gneiss containing shock veins in plane polarized transmitted light (a) and crossed polarizers (b). (c) Photomicrograph of planar shock features in orthoclase (Or) and quartz (Qtz) in crossed polarized light. (d) Secondary electron image of planar deformation features in quartz.

Fig. 3. Micro-faulted and sheared minerals in thin section. (a) BSE image showing offset and displacement of amphibole, orthoclase and plagioclase along a thin (~1 µm wide) shock vein. (b) Transmitted light image of the same vein shown in (a), rotated 45° clockwise. (c) BSE images of sheared epidote, (d) Reflected light image of deformation in quartz along a vein margin. Or = orthoclase, Pl = plagioclase, Prg = ferro-pargasite, Qtz = quartz.

Fig. 4. Phase transformation associated with shock veins. (a) Green ferro-pargasite (parg) is transformed to orange majoritic garnet along the shock vein margin. The shock vein matrix is opaque and forms an interlocking network (white arrows). (b) BSE image of orange garnet in (a) containing a complex network

of cracks. (c) The boundary between untransformed pargasite and shock-produced garnet is sharp, with fingers of garnet extending away from the shock vein margin into adjacent pargasite. (d) Micrometer-size euhedral garnet crystals that have crystallized from melt within the shock vein matrix. (e,f) TEM bright-field images of garnets embedded in a matrix of amorphous material and phyllosilicates. (h) Garnets poikilitically enclose nanometer circular features with layered structures that suggest glass inclusions partially altered to phyllosilicate. Or = orthoclase, Pl = plagioclase, Prg = ferro-pargasite, Qtz = quartz, Grt = almandine-majorite garnet.

Fig. 5. (a) BSE image showing the location of the FIB section extracted across the shock-transformed orange garnet along the vein margin and the shock vein matrix. The white arrow points to the crack visible in (b), which defines the boundary between the vein matrix and garnet. (b) TEM bright field image showing the entire FIB foil, corresponding to the area shown in (a). (c, d) TEM bright-field image of garnet along the vein margin. (c) Garnet looking down [111]. Note the complex matrix of material with vesiculated glass between crystals. (d) Nanometer size garnet fragments viewed along [001]. Note the vesicular glass between fragments, which appear to fit together. Inset, the SAED pattern of the garnet [001] zone axis. Grt = almandine-majorite garnet, Bt = biotite.

Fig. 6. Raman spectra from representative phases.

Fig. 7. Histogram comparing EMP data from ferro-pargasite with its shock-transformation product (garnet), represented as log mean wt% oxide versus oxide for major and minor elements. Each column represents the average wt% oxide from EMP data from 10 grains from three different areas of the thin section, collected using a fully focused (~1 µm diameter) electron beam on pargasite and orange garnet adjacent to one another along shock vein margins. Error bars are 1 σ.

Fig. 8. (a) Photograph of the cut surface of the ST003 core sampled at 377 m depth, which contains a thin shock vein (oriented roughly vertical) and a cross-cutting veinlet of polymict breccia. (b) Plane polarized light photograph showing the shock vein truncated by the veinlet. (c) BSE image of small angular fragments of the shock vein matrix, observed as 1–2 μm euhedral almandine garnet (inset), entrained within the breccia. Ab = albite, Qtz = quartz.

References

Akaogi M. and Akimoto S. (1977) Pyroxene-garnet solid solution equilibria in the systems $Mg_2Si_4O_{12}$-$Mg_3Al_2Si_3O_{12}$ and $Fe_4Si_4O_{12}$-$Fe_3Al_2Si_3O_{12}$ at high pressures and temperatures. *Phys. Earth Planet. Int.* **15**, 90-106.

Artemieva N.A., Wünnemann K., Krien F., Reimold U. and Stöffler D. (2013) Ries crater and suevite revisted – Observations and modeling Part II: Modeling. *Meteor. Planet. Sci.* **48**, 590-627. doi: 10.111/maps.12085

Baer M. R. (2000) Computational modeling of heterogeneous materials at the mesoscale. In *Shock Compression of Condensed Matter-2001* (M. D. Furnish et al., Eds.), AIP Conference Proceedings 505, American Institute of Physics, New York, pp. 27-33.

Baer M. R. and Trott W.M. (2002) Mesoscale descriptions of shock-loaded heterogeneous porous materials. In *Shock Compression of Condensed Matter-2001* (M. D. Furnish et al., Eds.), AIP Conference Proceedings 620, American Institute of Physics, New York, pp. 517-520.

Beck P., Gillet Ph., El Goresy A. and Mostefaoui S. (2005) Timescales of shock processes in chondritic martian meteorites. *Nature* **435**, 1071-1074. doi:10.1038/nature03616.

Biren M. B. and Spray J.G. (2011) Shock veins in the central uplift of the Manicouagan impact structure: context and genesis. *Earth Planet. Sci. Lett.* **303**, 310-322. doi: 10.1016/j.epsl.2011.01.003

Burwash R. A., McGregor C. R. and Wilson J.A. (1994) Precambrian basement beneath the Western Canada Sedimentary Basin. In Geological Atlas of the Western Canada Sedimentary Basin (G.D. Mossop and I. Stetson eds.), Canadian Society of Petroleum Geologists, Alberta Research Council, p. 49-56.

Carrigy M. A. and Short N.M. (1968) Evidence of shock metamorphism in rocks from the Steen River Structure, Alberta. In Shock Metamorphism of Natural Materials. B.M. French and N.M. Short (Eds.), Mono Book Corporation, Baltimore, pp. 367-378.

Chen M., Sharp T. G., El Goresy A., Wopenka B. and Xie X. (1996) The majorite-pyrope + magnesiowüstite assemblage: Constraints on the history of shock vein in chondrites. *Science* **271**, 1570-1573.

Chester J. S., Chester F. M. and Kronenberg A.K. (2005) Fracture surface energy of the Punchbowl Fault, San Andreas system. *Nature* **437**, 133-136.

Collerson K., Williams Q., Kamber B.S., Omori S., Arai H. and Ohtani E. (2010) Majoritic garnet: A new approach to pressure estimation of shock events in meteorites and the encapsulation of sub-lithospheric inclusions in diamond. *Geochim. Cosmochim. Acta* **74,** 5939-5957. Doi: 10.1016/j.gca.2010.07.005

Daniel I., Gillet P., McMillan P. F., Wolf G. and Verhelst M. A. (1997) High-pressure behaviour of anorthite: Compression and amorphization. *J. Geophys. Res.* **102**, 10,313-10,325.

Dence M. R., Grieve R. A. F. and Robertson P. B. (1977) Terrestrial impact structures: principal characteristics and energy considerations. In: Roddy, D.J., Pepin, R.O. Merrill R.B. (Eds.), Impact and Explosion Cratering. Pergamon Press, New York, pp. 247-275.

Dressler B. and Graup G. (1969) Pseudotachylite aus dem Nördlinger Ries. *Geol. Bav.* **60**, 170-171.

French B. M. (1998) Traces of catastrophe: a handbook of shock-metamorphic effects in terrestrial meteorite impact structures. LPI Contrib. 954, Lunar Planet. Inst., Houston, pp. 120.

Fritz J., Wünnemann K., Greshake A., Fernandes V.A.S.M., Boettger U. and Hornemann U. (2011a) Shock pressure calibration for lunar plagioclase. XLII Lunar Planet. Sci., Abstract #1196.

Fritz J., Wünnemann K., Reimold U., Meyer C. and Hornemann U. (2011b) Shock experiments on quartz targets pre-cooled to 77 K. *Int. J. Impact Eng.* **38**, 440-445. Doi: 10.1016/j.ijimpeng.2010.10.014

Gibson R.L. and Reimold W.U. (2005) Shock pressure distribution in the Vredefort impact structure, South Africa. In Kenkmann T. et al. eds., Large meteorite impacts and planetary evolution III: Geological Society of America Special Paper 384, pp. 329-349.

Gillet Ph., El Goresy A., Beck P. and Chen M. (2007) High-pressure mineral assemblages in shocked meteorites and shocked terrestrial rocks: Mechanisms of phase transformation and constraints to pressure and temperature histories. *Geol. Soc. Amer. Spec. Publ.* **421**, 57-82. Doi: 10.1130/2007.2421(05).

Grew E. S., Locock A. J., Mills S. J. Galuskina I. O., Galuskin E. V. and Hålenius U. (2013) IMA report: Nomenclature of the garnet supergroup*. Am. Miner***. 98**, 785-811.

Grieve R. A. F. (2006) Steen River. In: Grieve, R.A.F. (Ed.) Impact structures in Canada. Geological Association of Canada, Canada, pp. 210.

Griffin W. L. (2008) Major transformations reveal Earth's deep secrets. *Geol*. **36**, 95-96.

Heider N. and Kenkmann T. (2003) Numerical simulations of temperature effects at fissures due to shock loading. *Meteor. Planet. Sci.* **38**, 1451-1460.

Irifune T. (1987) An experimental investigation of the pyroxene-garnet transformation in a pyrolite composition and its bearing on the constitution of the mantle. *Phys. Earth Planet. Int.* **45**, 324-336.

Kenkmann T., Hornemann U. and Stöffler D. (2000) Experimental generation of shock-induced pseudotachylites along lithological interfaces. *Meteor. Planet. Sci*. **35**, 1275-1290.

Kubo T., Kimura M., Kato T., Nishi M., Tominaga A., Kikegawa T. and Funakoshi K. (2010) Plagioclase breakdown as an indicator for shock conditions of meteorites. *Nat. Geosci.* **3**, 41-45. Doi:10.1038/NGEO70.7

Langenhorst F. and Poirier J. -P. (2000) 'Eclogitic' minerals in a shocked basaltic meteorite. *Earth Planet. Sci. Lett.* **176**, 259-265.

Langenhorst F., Poirier J.-P., Deutsch A. and Hornemann U. (2002) Experimental approach to generate shock veins in single crystal olivine by shear melting. *Meteor. Planet. Sci.* **37**, 1541-1553.

Lieger D., Riller U. and Gibson R.L. (2009) Generation of fragment-rich pseudotachylite bodies during central uplift formation in the Vredefort impact structure, South Africa. *Earth Planet. Sci. Lett***. 279**, 53-54. Doi: 10.1016/j.epsl.2008.12.031.

Lowrinson G. C. (1974) Crushing and grinding. Ohio, CRC, pp. 286.

Locock A. (2008) An Excel spreadsheet to recast analyses of garnet into end-member components, and a synopsis of the crystal chemistry of natural silicate garnets. *Comp. & Geosci.* **34,** 1769-1780.

Locock A. (2014) An Excel spreadsheet to classify analyses of amphiboles following the IMA 2012 recommendations. *Comp. & Geosci.* **62**, 1-11.

Martini J. (1978) Coesite and stishovite in the Vredefort Dome, South Africa. *Nature* **272**, 715-717.

Martini J. (1991) The nature, distribution and genesis of the coesite and stishovite associated with the pseudotachylite of the Vredefort Dome, South Africa. *Earth Planet. Sci. Lett.* **103**, 285-300.

Molak B., Balzer S.A., Olson R.A. and Waters E.J. (2002) Petrographic, Mineralogical and Lithogeochemical study of core from three drillholes into the Steen River Structure, northern Alberta. Alberta Energy and Utilities Board, Earth Sci. Report 2001-04, 91 p.

Nishihara Y. and Takahashi E. (2001) Phase relation and physical properties of an Al-depleted komatiite to 23 GPa. *Earth Planet. Sci. Lett.* **190**, 65-77.

Ostertag T. (1983) Shock experiments on feldspar crystals. Proc. Lunar Planet. Sci. Conf. 14th, J. Geophys. Res. 89, B631-B640.

Reimold W. U. (1998) Exogenic and endogenic breccias: a discussion of major problematics. *Earth-Sci. Rev.***43,** 25-47.

Ringwood A. E. (1967) The pyroxene garnet transformation in the Earth's mantle. *Earth Planet. Sci. Lett.* **2,** 255-263.

Sajeev K., Osanai Y., Kon Y. and Itaya T. (2009) Stability of pargasite during ultrahigh-temperature metamorphism: A consequence of titanium and REE partitioning? *Am. Miner.* **94**, 535-545. doi: 10.2138/am.2009.2815.

Sharp T. G. and DeCarli P. S. (2006) Shock effects in meteorites. In Meteorites and the early Solar System (eds. D.S. Lauretta and H.Y. McSween, Jr). The University Press, Tucson, pp. 653-678.

Shaw C. S. J. and Walton E.L. (2013) Thermal modeling of shock melts in a heavily shock metamorphosed L6 chondrite. Meteor. Planet. Sci., Abstract #5153.

Spray J. G. (1998) Localized shock- and friction-induced melting in response to hypervelocity impact. *Geol. Soc. Lond. Spec. Pub.* **140**, 195-204.

Spray J. G. (2010) Frictional melting processes in planetary materials: from hypervelocity impact to earthquakes. *Annu. Rev. Earth Planet. Sci*. **38**, 221-254. Doi:10.1146/annurev.earth.03108.100045

Stachel T. (2001) Diamonds from the asthenosphere and the transition zone. *Eur. J. Miner*. **13**, 883-892.

Stähle V., Altherr R., Nasdala L. and Ludwig T. (2011) Ca-rich majorite derived from high-temperature melt and thermally stressed hornblende in shock veins of crustal rocks from the Ries impact crater (Germany). *Contrib. Miner. Petrol.* **161**, 275-291.

Steiger R.H. and Jager E. (1977) Subcommission on geochronology: Convention on the use of decay constants in geo- and cosmochronology. *Earth Planet. Sci. Lett.* **36**, 359-362.

Stöffler D. (1971) Progressive metamorphism and classification of shocked and brecciated crystalline rocks at impact craters. *J. Geophys. Res.* **76**, 5541-5551.

Stöffler D. (1974) Deformation and transformation of rock-forming minerals by natural and experimental shock processes II. Physical properties of shocked minerals. *Fortchr. Miner.* **51**, 256-289.

Stöffler D. (1984) Glasses formed by hypervelocity impact. *J. Non-Crystalline Solids* **67**, 465-502.

Stöffler D. and Grieve R. A. F. (2007) Impactites In Metamorphic rocks: a classification and glossary of terms, recommendations of the IUGS, Cambridge University Press, Cambridge, UK, 82-92, 111-125 and 126-242.

Stöffler D., Artemieva N., Wünnemann K., Reimold U., Jacob J., Hansen B. K. and Summerson I. A.T. (2013) Ries crater and suevite revisited – Observations and modeling Part I: Observations. *Meteor. Planet. Sci.* **48**, 515-589.

Tomioka N. and Fujino K. (1997) Natural (Mg,Fe)SiO_3-ilmenite and -perovskite in the Tenham meteorite. *Science* **277,** 1084-1086. Doi: 10.1126/science.277.5329.1084.

Tomioka N., Kondo H., Kunikata A. and Nagai T. (2010) Pressure-induced amorphization of albitic plagioclase in an externally heated diamond anvil cell. *Geophys. Res. Lett.* **37**, L21301. Doi: 10.1029/2010GL044221.

Tschauner O., Ma C., Beckett J. R., Prescher C., Prakapenka V. B. and Rossman G. R. (2014) Discovery of bridgmanite, the most abundant mineral in Earth, in a shocked meteorite. *Science* **346**, 1100-1102. Doi: 10.1126/science.1259369.

Treiman A. H. (1998) The history of Allan Hills 84001 revised: multiple shock events. *Meteor. Planet. Sci.* **33**, 753-764.

Walton E.L., Spray J. G. and Bartoschewitz R. (2005) A new martian meteorite from Oman: Mineralogy, petrology and shock metamorphism of olivine-phyric basaltic shergottite Sayh al Uhaymir 150. *Meteor. Planet. Sci.* **40**, 1195-1214.

Walton E. L., Sharp T. G. and Hu J. (2014) Heterogeneous mineral assemblages in martian meteorite Tissint as a result of a recent small impact crater on Mars. *Geochim. Cosmochim. Acta* **140**, 334-348.

Walton E. L., Hughes A. and Herd C. D. K. (2015) Previously unrecognized impactites from the Steen River impact structure, NW Alberta, Canada: A new variety of suevite? 46th LPSC, Abstract #2592.

Winzer S. R. (1972) The Steen River Astrobleme, Alberta, Canada. 4th Int. Geol. Cong., Proc., Section 15, 148-156.

Xirouchakis D., Draper D. S. and Agee C. B. (2002) The garnet to majorite transformation in mafic compositions. XXXIII Lunar Planet. Sci., Abstract #1316.

Xie Z., Sharp T. G. and DeCarli P. S. (2006) High-pressure phases in a shock-induced melt vein of the Tenham L6 chondrite: constrains on shock pressure and duration. *Geochim. Cosmochim. Acta* **70**, 504–515.

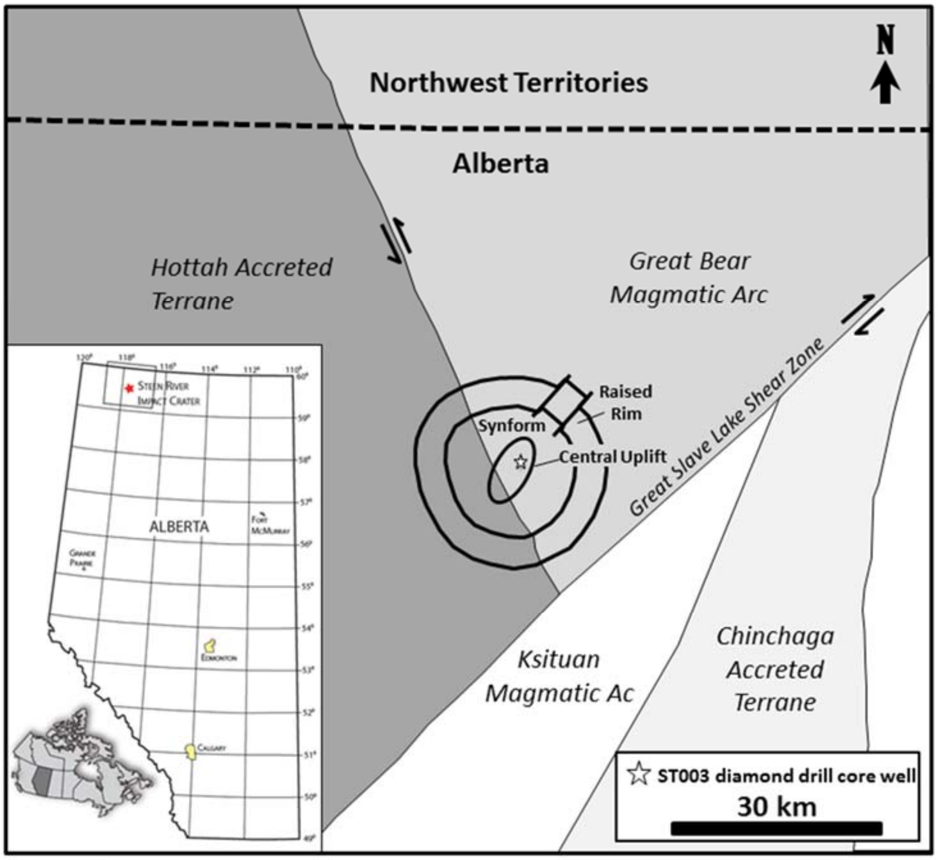
N
Northwest Territories
Alberta
Hottah Accreted Terrane
Great Bear Magmatic Arc
Great Slave Lake Shear Zone
Raised Rim
Synform
Central Uplift
Ksituan Magmatic Ac
Chinchaga Accreted Terrane
ST003 diamond drill core well
30 km
Steen River Impact Crater
ALBERTA
Fort McMurray
Grande Prairie
Edmonton
Calgary

Figure 1

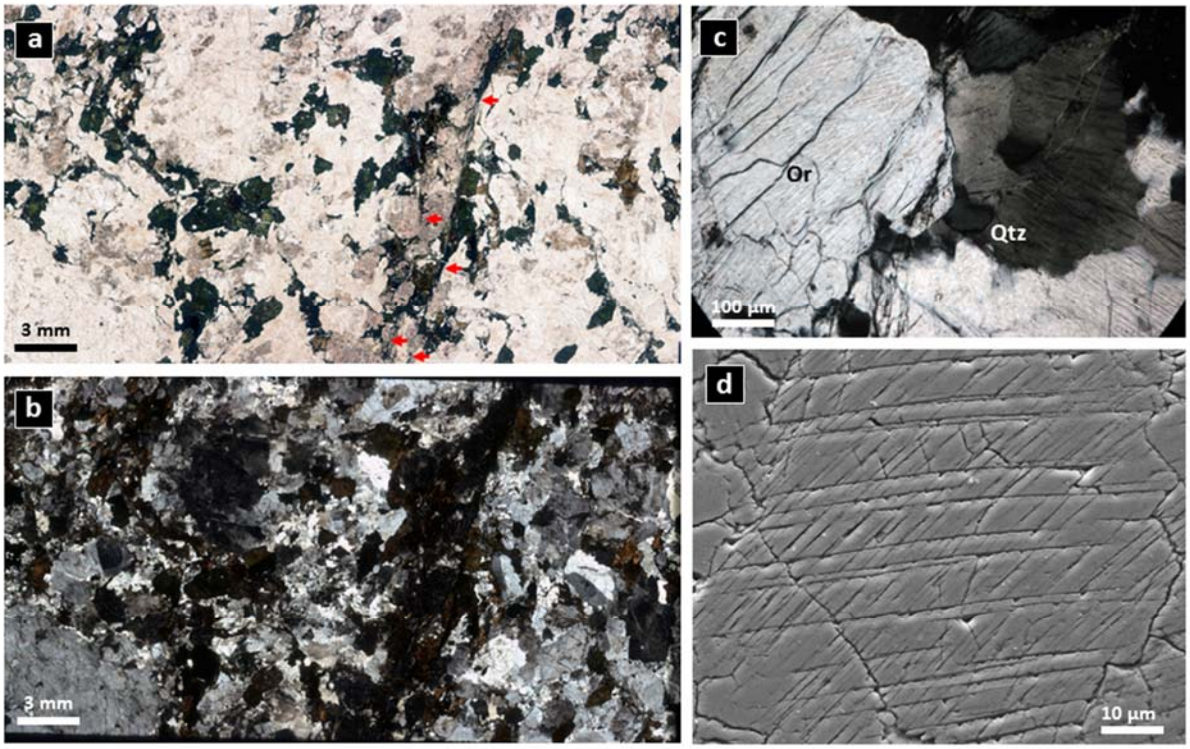

Figure 2

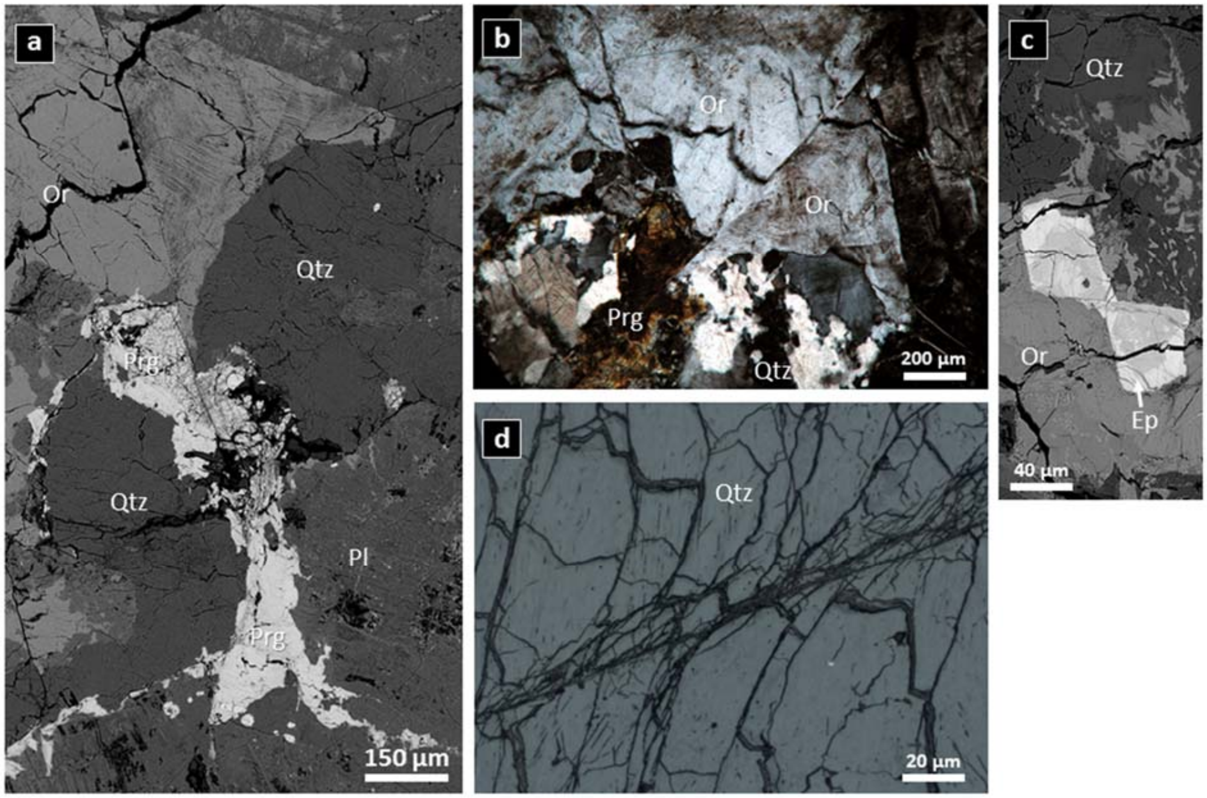
a
Or
Qtz
Prg
Qtz
Pl
Prg
150 µm
b
Or
Or
Prg
Qtz
200 µm
c
Qtz
Or
Ep
40 µm
d
Qtz
20 µm

Figure 3

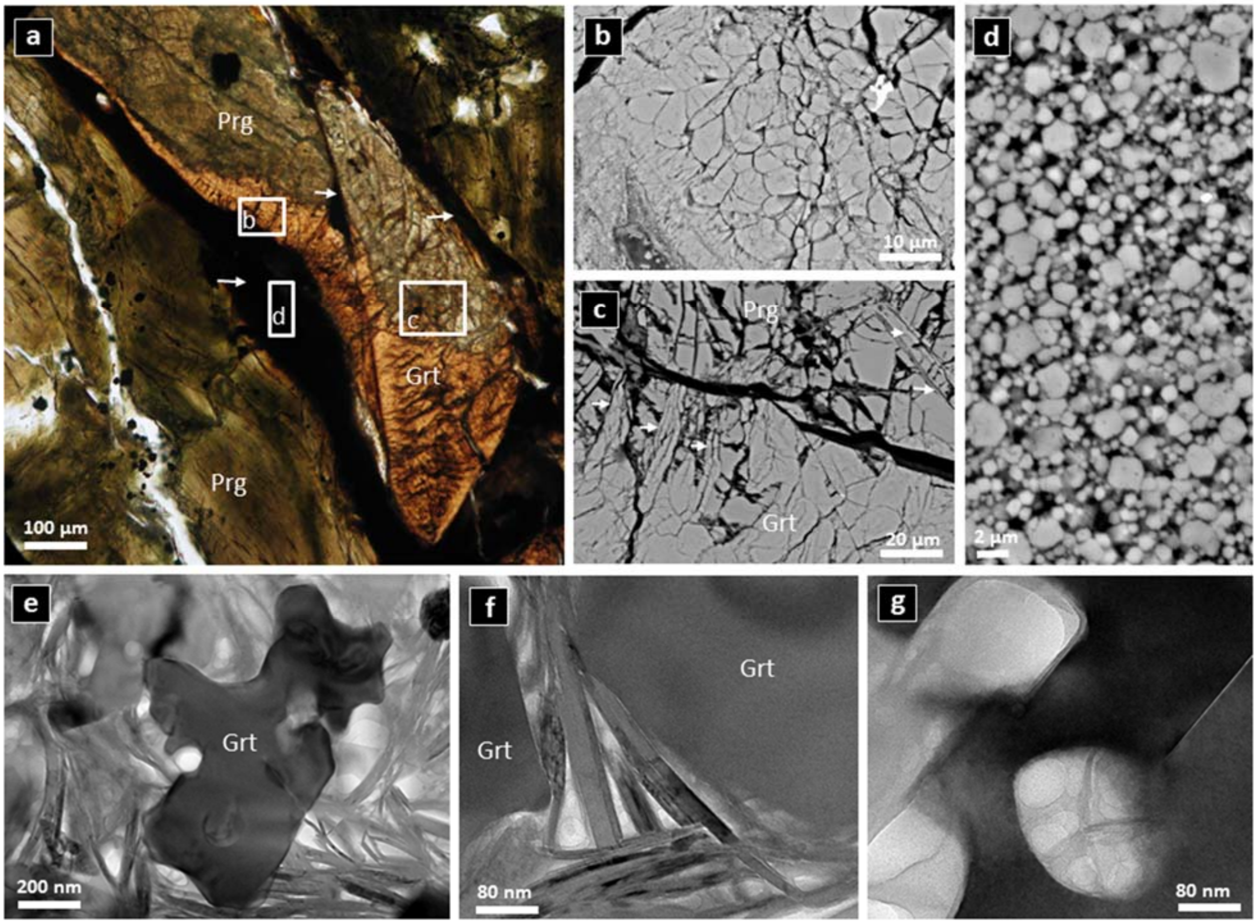
a
Prg
b
d
c
Grt
Prg
100 µm
b
10 µm
c
Prg
Grt
20 µm
d
2 µm
e
Grt
200 nm
f
Grt
Grt
80 nm
g
80 nm

Figure 4

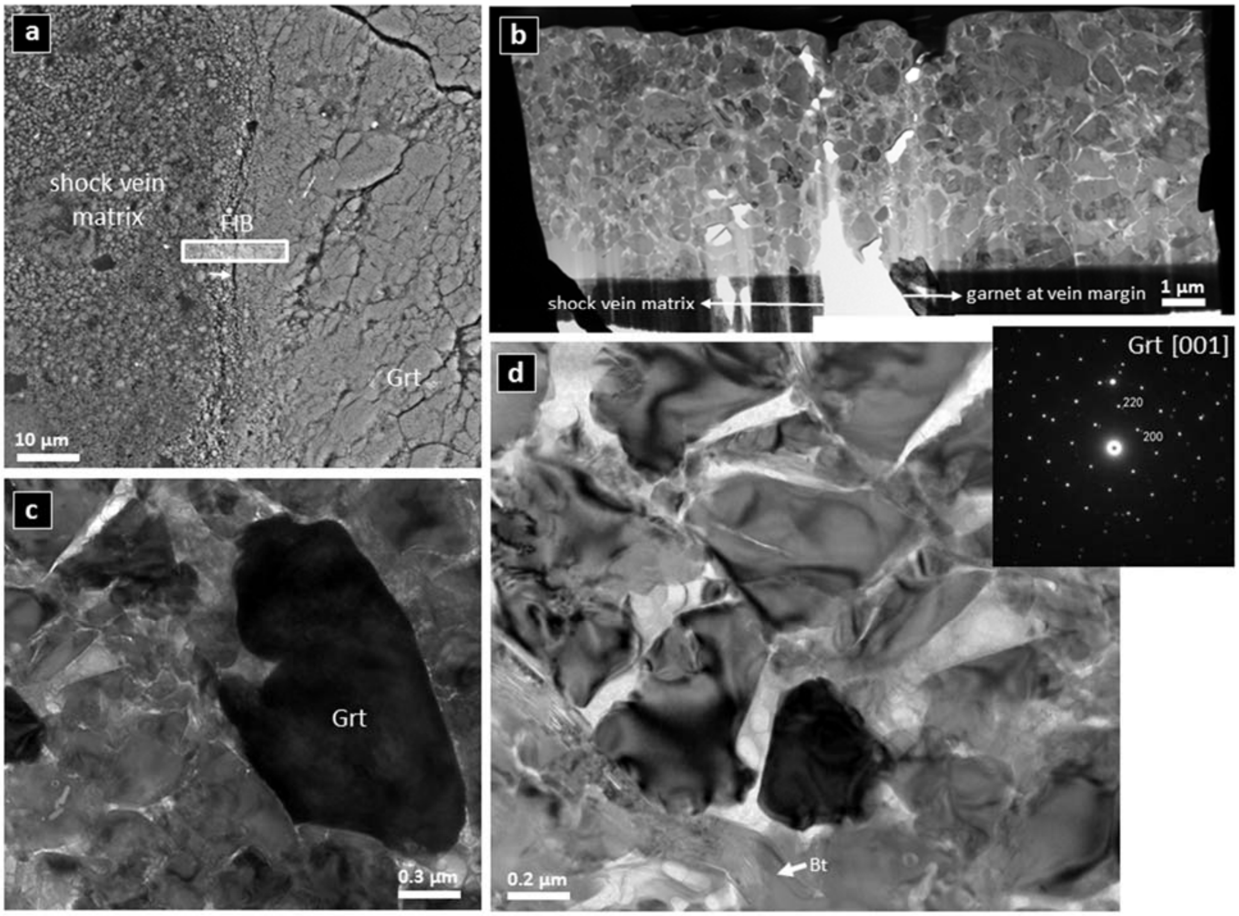
a
shock vein
matrix
FIB
Grt
10 µm
b
shock vein matrix
garnet at vein margin
1 µm
c
Grt
0.3 µm
d
Grt [001]
220
200
Bt
0.2 µm

Figure 5

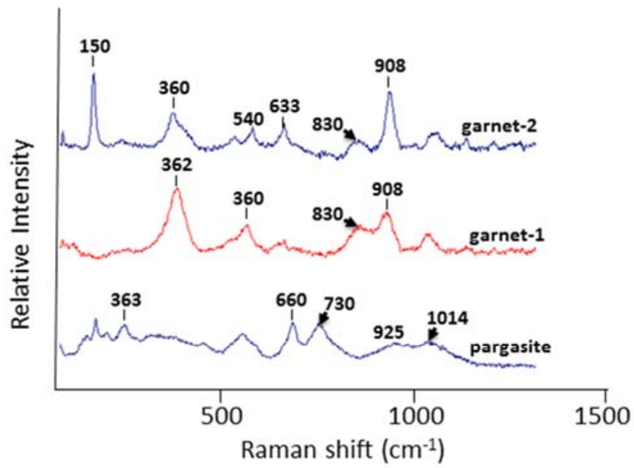
150
360
540
633
830
908
garnet-2
362
360
830
908
garnet-1
363
660
730
925
1014
pargasite
Relative Intensity
500
1000
1500
Raman shift (cm-1)

Figure 6

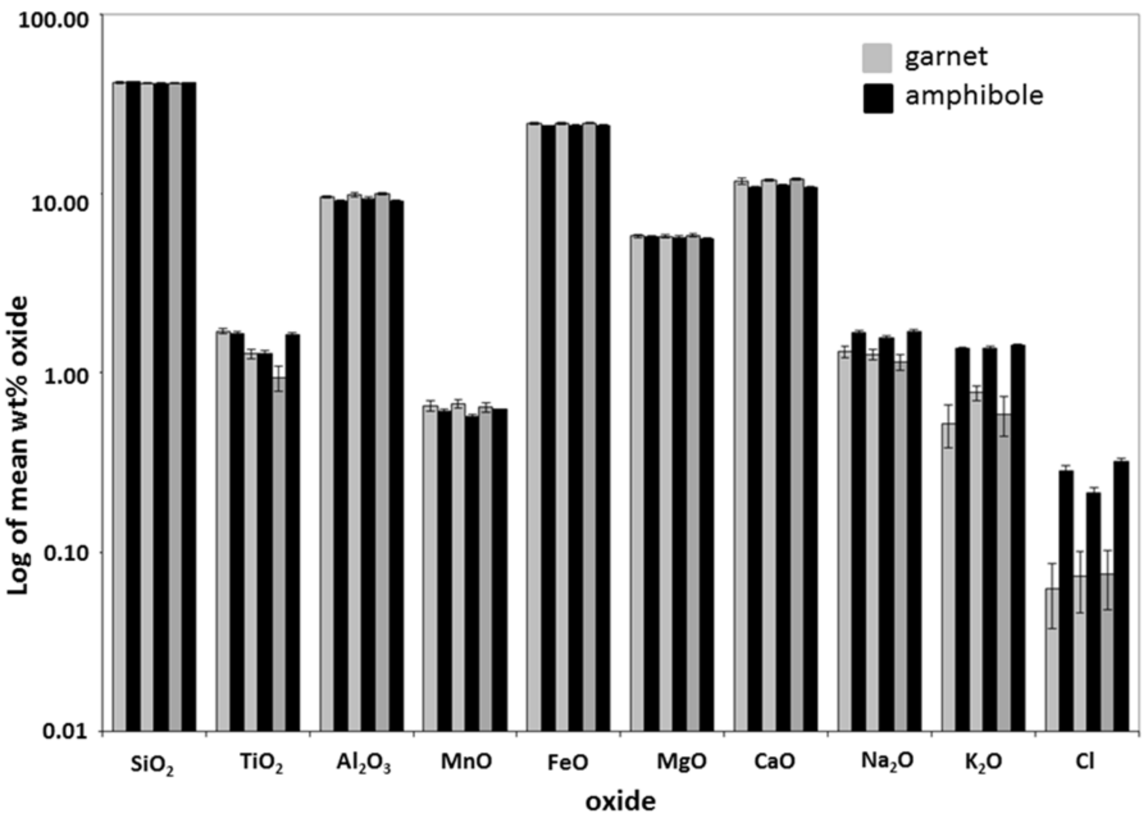

100.00
10.00
1.00
0.10
0.01
Log of mean wt% oxide
garnet
amphibole
SiO2
TiO2
Al2O3
MnO
FeO
MgO
CaO
Na2O
K2O
Cl
oxide

Figure 7

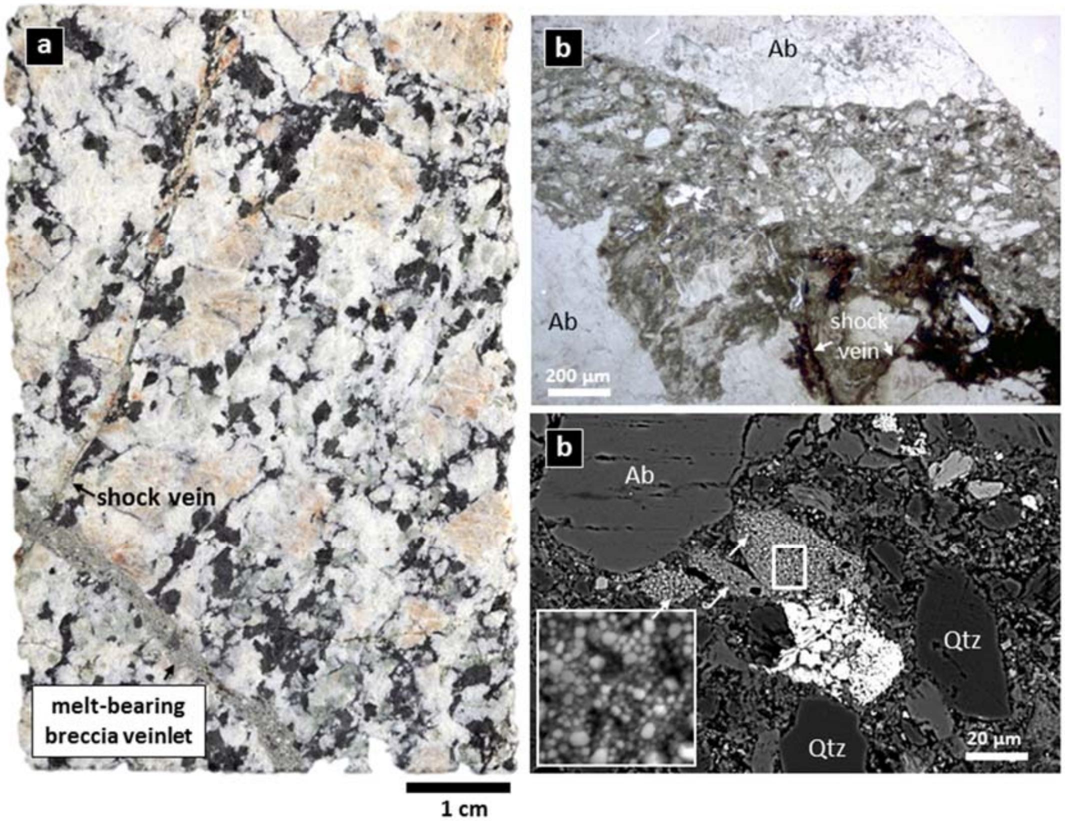
a
shock vein
melt-bearing
breccia veinlet
1 cm
b
Ab
Ab
shock
vein
200 µm
b
Ab
Qtz
Qtz
20 µm

Figure 8

Table 1

Representative electron microprobe analyses of major minerals in crystalline rocks sampled at 378 m depth within ST003 drill core

Oxide	Pl	σ	Or	σ	Prg	σ	Bt	σ	Grt-1	σ	Grt-2	σ
SiO_2	61.1	0.32	64.9	0.34	41.2	0.39	34.9	0.38	42.4	0.35	40.6	0.56
TiO_2	b.d.	0.01	b.d.	0.01	1.68	0.19	3.89	0.97	1.62	0.33	0.55	0.14
Al_2O_3	24.6	0.09	19.0	0.08	9.6	0.19	14.5	0.52	9.8	0.22	19.9	0.49
FeO	0.08	0.01	0.05	0.00	25.1	0.16	26.7	0.62	24.4	0.32	24.8	1.35
MnO	b.d.	0.01	b.d.	0.00	0.70	0.10	0.3	0.02	0.62	0.04	0.44	0.03
MgO	b.d.	0.01	b.d.	0.05	5.6	0.17	6.8	0.49	6.0	0.11	11.1	1.38
CaO	5.8	0.02	0.03	0.05	11.1	0.08	b.d.	–	11.9	0.35	0.74	0.17
Na_2O	8.2	0.50	2.4	0.28	1.25	0.04	0.21	0.08	1.45	0.11	0.32	0.09
K_2O	0.2	0.01	13.5	0.37	0.71	0.05	9.6	0.89	0.41	0.16	0.72	0.32
Cl	n.a.	–	n.a.	–	0.31	0.05	0.03	0.01	0.07	0.03	0.10	0.03
Total	99.98		99.88		97.25		96.93		98.67		99.27	
Formula												
O =	8		8		22		22		12		12	
Si	2.717		2.977		6.596		2.789		3.369		3.108	
Ti	0.000		0.000		0.197		0.233		0.097		0.027	
Al	1.289		1.026		1.697		1.362		0.922		1.815	
Fe^{2+}	0.003		0.002		3.041		1.779		1.255		1.540	
Fe^{3+}	0.000		0.000		0.139		0.000		0.369		0.000	
Mn	0.000		0.000		0.079		0.020		0.041		0.030	
Mg	0.000		0.000		1.331		0.808		0.712		1.363	
Ca	0.273		0.002		1.810				1.011		0.054	
Na	0.703		0.211		0.514		0.033		0.224		0.036	
K	0.010		0.788		0.274		0.975		0.000		0.000	
Total	4.994		5.005		15.678		7.999		8.000		7.973	
An	27.7		0.2									
Ab	71.3		21.1									
Or	1.0		78.8									
n	20		10		32		8		36		6	

Pl= plagioclase, Or = orthoclase, Prg = ferro-pargasite amphibole, Bt = biotite, Grt-1 = orange garnet along shock vein margins,
Grt -2 = garnet within shock vein matrix, n.a.= not analyzed, b.d. = below detection limits